Ultrafast synthesis of L-His-Fe₃O₄ nanozymes with enhanced peroxidase-like activity for effective antibacterial applications

Ye Yuan[1,2†], Yuan Liu[1,2†], Zhipeng Shen[1], Huidan Wu[1], Lantian Meng[1], Xiaoxiao Guo[1], Bing Jiang[1,2]* and Ling Fang[3,4]*

[1]Nanozyme Laboratory in Zhongyuan, School of Basic Medical Sciences, Zhengzhou University, Zhengzhou, China, [2]Nanozyme Laboratory in Zhongyuan, Henan Academy of Innovations in Medical Science, Zhengzhou, Henan, China, [3]Department of Dermatology, Xishan People's Hospital of Wuxi City, Wuxi Branch of Zhongda Hospital Southeast University, Wuxi, Jiangsu, China, [4]Jiangsu Institute of Parasitic Diseases, Wuxi, Jiangsu, China

Background: Bacterial resistance remains a significant challenge, necessitating the development of new antibacterial strategies. This study introduces a rapidly synthesized L-histidine- Fe₃O₄ (L-His-Fe₃O₄) nanozyme with enhanced peroxidase (POD)-like activity, designed to improve antibacterial efficacy and accelerate the healing of bacteria-infected wounds.

Methods: We successfully synthesized L-His-Fe₃O₄ using an ultrafast, room-temperature synthesis method, and observed its anti-infection effect and explored its anti-infection mechanism through *in vivo* and *in vitro* antibacterial experiments.

Results: We produced L-His-Fe₃O₄ cost-effectively while preserving L-His, which was essential for its catalytic and antibacterial functions. The resulting nanozyme demonstrated exceptional antibacterial activity against both Gram-positive (*S. aureus*) and Gram-negative (*E. coli*) bacteria. *In vivo* experiments revealed that L-His-Fe₃O₄ outperformed vancomycin in reducing bacterial viability and effectively promoting wound healing, all while maintaining excellent biosafety with no adverse effects on blood or liver functions.

Discussion: These findings highlight the potential of L-His-Fe₃O₄ for large-scale production and practical use in treating bacterial infections, offering a promising approach to combating antibiotic-resistant pathogens.

KEYWORDS

nanozyme, antibacterial, l-histidine, Fe₃O₄, biofilm

1 Introduction

The misuse and overuse of antibiotics have led to an alarming rise in multidrug-resistant bacteria, posing a severe threat to global public health (Brown and Wright, 2016; Pogue et al., 2015). Infections such as tuberculosis and gonorrhea are increasingly challenging to treat due to this resistance (Alim-Marvasti et al., 2016; Lee et al., 2020). Unfortunately, the development of new antibiotics has lagged behind

the rapid emergence of bacterial resistance (Theuretzbacher et al., 2020; Brussow, 2024; Burki, 2018). The World Health Organization (WHO) predicts that by 2050, antibiotic resistance could result in up to 10 million deaths annually, identifying it as one of the top ten global threats to humanity (He et al., 2014). To address bacterial resistance, researchers have explored various novel antibacterial strategies (Panda et al., 2018; Gupta et al., 2019; Li et al., 2019; Makabenta et al., 2021), including antimicrobial peptides, bacteriophages, probiotics, and plant extracts; however, much of this research remains in its early stages.

In recent years, advancements in nanotechnology have led to the application of nanomaterials in medicine (Fan et al., 2021; Wang et al., 2018; Seaberg et al., 2023; Gao et al., 2007). In 2007, the Yan group demonstrated that Fe_3O_4 possesses peroxidase-like activity (Gao et al., 2024; Xie et al., 2024), paving the way for the development of nanozymes-nanomaterials with enzyme-like catalytic properties (Jiang et al., 2019; Sheng et al., 2024). Due to their adjustable physicochemical properties and unique catalytic activities, nanozymes hold significant promise for antibacterial applications (Liu et al., 2024). They can effectively kill bacteria by generating reactive oxygen species (ROS), such as hydroxyl radicals ($\cdot OH$) and superoxide anions ($\cdot O_2^-$) (Song et al., 2024; Trujillo-Alonso et al., 2019). Numerous studies have reported various nanozymes for antibacterial purposes, with Fe_3O_4 receiving FDA approval for biomedical applications, highlighting its high biosafety profile (Wei et al., 2021). Consequently, Fe_3O_4 emerges as a particularly promising candidate in combating bacterial infections. However, the primary synthesis methods for Fe_3O_4 like hydrothermal and solvothermal approaches are often tedious, time-consuming, expensive, and high temperature, which hinders large-scale production (Dong et al., 2022; Liu et al., 2021). Thus, there is an urgent need to improve Fe_3O_4 synthesis methods to accelerate the development of new antibacterial agents.

In this work, we present a low-cost and ultrafast method for synthesizing Fe_3O_4 to enhance its antibacterial properties. The synthesis of Fe_3O_4 at room temperature can preserve the structure and biological function of the modified histidine (L-His), thereby enhancing its antibacterial properties. In detail, by mixing ferrous chloride and L-His in an ammonium hydroxide solution for only 1 minute, we successfully synthesized L-His-Fe_3O_4. This method leverages histidine's ability to enhance peroxidase (POD)-like activity through its activation of hydrogen peroxide reduction reactions (Yang et al., 2019; Du et al., 2022). Notably, this reaction occurs at room temperature, preserving the functional integrity of L-His. The improved POD-like activity of L-His-Fe_3O_4 catalyzed the production of hydroxyl radicals ($\cdot OH$), which disrupt bacterial cell membranes and degrade biofilms. Both *in vitro* and *in vivo* antibacterial tests demonstrated the strong antimicrobial efficacy of L-His-Fe_3O_4. In wound healing studies, L-His-Fe_3O_4 exhibited a superior capacity to promote healing compared with vancomycin. Additionally, L-His-Fe_3O_4 showed excellent biosafety, reinforcing its potential as a novel antibacterial agent. Moreover, the synthesis strategy of L-His-Fe_3O_4 at room temperature provide a new pathway for complete modification of different functional groups of Fe_3O_4.

2 Materials and methods

2.1 Chemical reagents, bacteria, and animals

Ferrous chloride ($FeCl_2$) and L-His were purchased from Sigma and Beyotime, respectively. Ammonium hydroxide was obtained from J&K Scientific. MRSA (ATCC 43300) and *S. aureus* (ATCC 29213) were sourced from the American Type Culture Collection (ATCC), and *E. coli* (CCUG58541) was obtained from the BeNa Culture Collection (BNCC). Balb/c mice were purchased from Qinglongshan Laboratory Animal Center. Fresh O-type red blood cells from Wuxi Central blood bank. Yeast extract (LP0021), glucose, and starch were obtained from Oxoid (UK). Dimethyl sulfoxide (DMSO) and agar were purchased from Sangon Biotech (China). Cell Counting Kit-8, crystal violet, and hydrogen peroxide (H_2O_2) were acquired from Aladdin Chemistry (Shanghai, China). Propidium iodide (PI) and Reactive Oxygen Species Assay Kit were sourced from Beyotime Biotechnology (Shanghai, China), while SYTO (Panda et al., 2018) green fluorescent nucleic acid stain was obtained from Thermo Fisher Scientific (Waltham, MA).

2.2 Theoretical calculation

Calculations were performed using the CP2K 2024.1 program. In the geometry optimization, Basis Set Superposition Error (BSSE) correction, and single-point calculations, the PBE-D3(BJ) functional was employed, incorporating Grimme's dispersion correction (D3) and the Becke-Johnson (BJ) damping factor. The DZVP-MOLOPT-SR-GTH basis set and the TZVP-MOLOPT-SR-GTH basis set were used for optimization and single-point calculations, respectively. Optimization continued until atomic forces were less than 0.02 eV/Å, with the self-consistent electronic energy convergence criterion set at 10^{-6} eV. Multiwfn 3.8 Dev was used for computational analysis, and visualization was performed with VESTA and Visual Molecular Dynamics (VMD) 1.9.3.

2.3 Bacterial strains and growth conditions

S. aureus and *E. coli* were cultured in LB medium, composed of 10 g of tryptone, 5 g of yeast extract, 10 g of sodium chloride, and 15–20 g of agar powder for solid medium. Agar plates and liquid cultures were incubated at 37°C, and frozen stocks of strains were stored at −80°C in LB containing 30% (v/v) glycerol.

2.4 *In Vitro* antibacterial assays

A colony of *S. aureus* or *E. coli* was randomly selected from LB agar plates, inoculated into 5 mL of LB culture, and incubated at 37°C for 12–18 h. After 24 h, the required amount of *S. aureus* or *E. coli* bacterial solution was transferred into fresh medium at a 1:100 ratio and cultured at 37°C for 4–6 h. When the OD_{600} reached 0.5, 100 μL of bacterial inoculum was mixed with H_2O (900 μL) as the control, while the experimental groups included L-His-Fe_3O_4, L-His-Fe_3O_4 + H_2O_2, and H_2O_2. After incubation at 37°C for a specified time, bacterial viability was assessed by plating bacteria

with appropriate dilution and calculating the colony-forming units per mL (CFU/mL). The fluorescent probe DCFH-DA was used to assess lipid peroxidation levels in the bacteria.

2.5 Observation by confocal laser microscopy (CLSM)

To facilitate observation of *S. aureus* biofilm changes, biofilms were cultured on a specialized cell climbing plate in a 24-well format, following previous *S. aureus* biofilm culture methods. Tryptone soy broth (TSB) was used as the medium. The procedure is as follows.

(1) A sterile cell pad was placed at the bottom of a well in a 24-well plate, and 2.8 mL TSB culture solution was added and incubated for 30 min before discarding the TSB.

(2) *S. aureus* solution was diluted with TSB to an OD_{600} of 0.5 at a 1:100 ratio, with 2.5 mL added per well, and incubated at 37°C for 24 h. To maintain a humid environment conducive to biofilm growth, saline was added to the remaining empty wells.

(3) Once the biofilm matured, the specified treatment substance was added. The culture solution and non-adherent bacteria were gently removed, and each well was washed twice with 2.5 mL PBS. The treatment was then applied for 3 h.

(4) For laser confocal observation, bacterial cells within the biofilm were stained with SYTO9/PI using a double-labeled fluorescence method and observed under a confocal laser microscope (SYTO9 = 0.5 μM; PI = 1 μM).

2.6 Inner and outer membrane permeability test

8-aniline-1-naphthalenesulfonic acid (ANS) has a non-polar benzene ring, which binds to the membrane lipid at the lipid-water junction. The fluorescence intensity of ANS is related to the fluidity of the polar region of the membrane lipid. Membrane permeability was assessed using the ANS uptake method. A solution of 20 μM ANS and *S. aureus* (10^7 CFU/mL) was prepared in 0.9% NaCl and incubated in darkness for 30 min. After centrifugation at 5000 g for 5 min, samples were washed and re-suspended in 0.9% NaCl. Fluorescence emission was measured at 450–600 nm with excitation at 380 nm. 3, 3′-Dipropylthiadicarbocyanine Iodide [diSC3(5)], a (C3) short alkyl tail carbonyl cyanine dyes, this kind of cationic dye can be used to detect and measure caused by membrane modification reagent across membrane potential or structural changes. Depolarization measurements were performed using diSC3(5) uptake with similar processing steps [diSC3(5), 4 μM; 622 nm excitation, 670 nm emission].

2.7 TEM (transmission electron microscope) and SEM (scanning electron microscope)

For each group, 0.5 mL of bacterial suspension (1.0×10^9 CFU/mL) was added to a 1.5 mL aseptic centrifuge tube along with 0.5 mL of ultra-pure water, H_2O_2, or L-His-Fe_3O_4 + H_2O_2. Each group's bacterial solution was incubated at 37°C for 3 h. After incubation,

samples were centrifuged and washed twice with ultra-pure water. The bacterial precipitate was then mixed with 2.5% glutaraldehyde solution and fixed at 4°C for 24 h. Bacterial morphology was observed and photographed using TEM and SEM.

2.8 Crystal violet staining

2.8.1 Cell culture

S. aureus solution with OD_{600} = 0.5 was diluted with biofilm culture medium (TSB) at a ratio of 1:100, with 100 μL added per well. Cultures were incubated at 37°C with 5% CO_2 for 24 h.

2.8.2 Add test compound

A medium containing the appropriate concentration of the test compound was added, and the cell culture plate was incubated for the specified time. Rinsing to remove floating bacteria: Methanol was used to rinse off floating bacteria, followed by a 15-min fixation with methanol, samples were then air-dried before staining.

2.8.3 Crystal violet

1 mL of 0.1% crystal violet solution was added to each well and stained for 15 min. Excess stain was rinsed off with distilled water. Dissolution of Crystal Violet: 33% glacial acetic acid was added to dissolve the crystal violet.
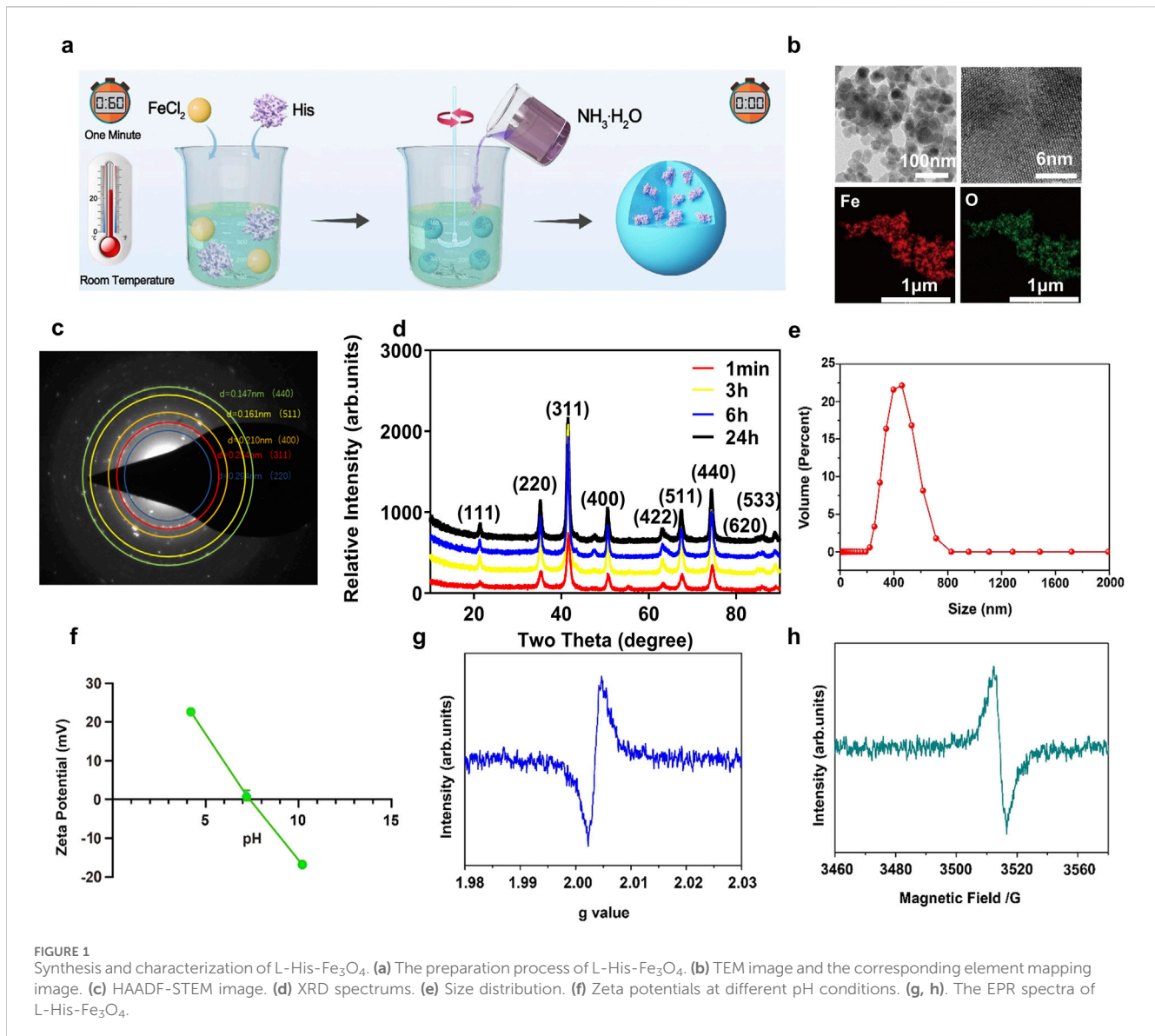
2.9 *In vitro* safety evaluation

HaCaT cells were inoculated into 96-well plates at a density of 5×10^3 cells per well and cultured in a serum-containing medium for 24 h (37°C, 5% CO_2). Culture medium containing varying concentrations of L-His-Fe_3O_4 (0, 100, 200, 400, 500 μg/mL) was then applied for 24 and 48 h. The medium was discarded, cells were washed once with PBS, and then cultured with CCK-8 for 3–4 h. After incubation, the 96-well plates were centrifuged (1,000 rpm for 5 min), 100 μL of supernatant was pipetted, and absorbance was measured at 490 nm.

2.10 Red blood cell hemolysis test

Fresh O-type red blood cells from Wuxi Central blood bank (Ethics Committee of Jiangsu Institute of Parasitic Diseases: JIPD-2022-005). An appropriate amount of human red blood cells was obtained and diluted fivefold with PBS buffer to prepare a red blood cell suspension. A 20 μL aliquot of the diluted suspension was mixed with different concentrations of L-His-Fe_3O_4. Triton X-100 and PBS buffer were used as positive and negative controls, respectively. All samples were incubated at 37°C for 2 h, then centrifuged at 1,000 rpm for 5 min. Photos were taken, and the supernatant was transferred to a 96-well plate for absorbance measurement at 540 nm.

2.11 *In vivo* safety assessment

Mouse wounds were treated externally with L-His-Fe_3O_4 once daily for seven consecutive days. After this period, histopathological

FIGURE 1
Synthesis and characterization of L-His-Fe$_3$O$_4$. **(a)** The preparation process of L-His-Fe$_3$O$_4$. **(b)** TEM image and the corresponding element mapping image. **(c)** HAADF-STEM image. **(d)** XRD spectrums. **(e)** Size distribution. **(f)** Zeta potentials at different pH conditions. **(g, h)**. The EPR spectra of L-His-Fe$_3$O$_4$.

sections of major organs (heart, liver, spleen, lung and kidney) were prepared for HE staining and photographed under the bright-field mode of a fluorescence microscope.

2.12 Animal experiment

Male Balb/c mice (20–25 g, 6–7 weeks of age) were randomly divided into four groups (n = 8), consisting of (1) control, (2) vancomycin (2 mg/mL, 20 μL), (3) hydrogen peroxide, and (4) L-His-Fe$_3$O$_4$ + H$_2$O$_2$ (2 mg/mL, 20 μL). After shaving, mice were anesthetized, and a circular wound approximately 0.8 cm in diameter was created on the back using surgical scissors. MRSA (1.0×10^8 CFU/mL) was then applied. After 24 h, an animal model of wound infection was established. Treatments were administered daily for the first 7 days following infection. On the 7th day, three mice from each group were randomly selected, wound tissue was collected, ground, diluted, and plated to observe *S. aureus* counts by
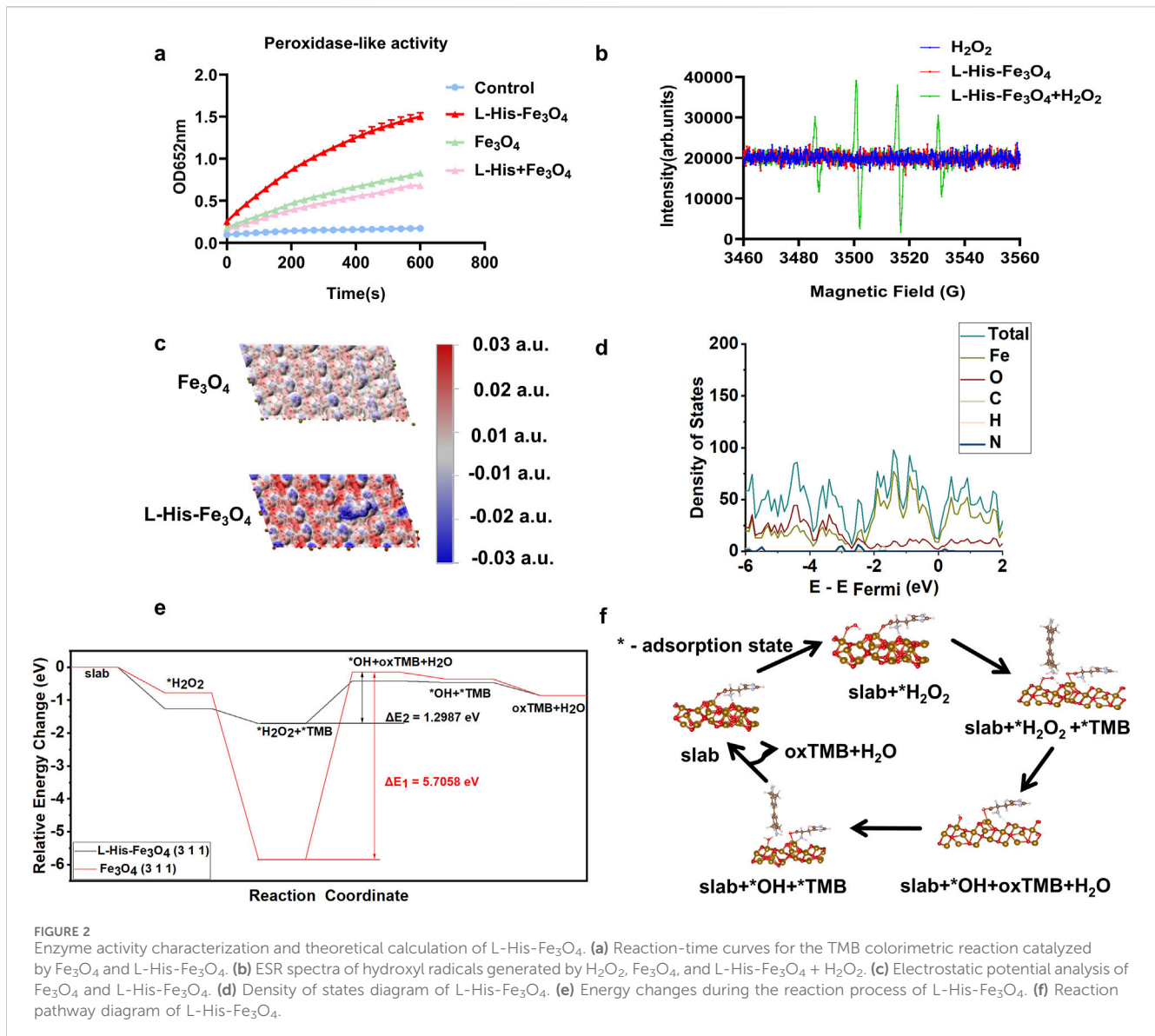
plate counting. Photos of wounds were taken on days 1, 3, 5, 7, 9 and 11 to document changes and measure wound size. Mice were euthanized, and organs and wound tissues were collected for hematoxylin-eosin (H&E) staining and Masson analysis.

3 Results

3.1 The synthesis and characterization of L-His-Fe$_3$O$_4$

L-His-Fe$_3$O$_4$ was synthesized by stirring at room temperature for 1 min. Briefly, ferrous chloride and L-His solutions were mixed, followed by the addition of 28% ammonium hydroxide. After stirring at room temperature for 1 min and drying at 60°C, L-His-Fe$_3$O$_4$ was obtained (Figure 1a). The yield of L-His-Fe$_3$O$_4$ is 36.48%, the morphology of L-His-Fe$_3$O$_4$ was observed by transmission electron microscopy (TEM). As shown in Figure 1b,

FIGURE 2
Enzyme activity characterization and theoretical calculation of L-His-Fe$_3$O$_4$. **(a)** Reaction-time curves for the TMB colorimetric reaction catalyzed by Fe$_3$O$_4$ and L-His-Fe$_3$O$_4$. **(b)** ESR spectra of hydroxyl radicals generated by H$_2$O$_2$, Fe$_3$O$_4$, and L-His-Fe$_3$O$_4$ + H$_2$O$_2$. **(c)** Electrostatic potential analysis of Fe$_3$O$_4$ and L-His-Fe$_3$O$_4$. **(d)** Density of states diagram of L-His-Fe$_3$O$_4$. **(e)** Energy changes during the reaction process of L-His-Fe$_3$O$_4$. **(f)** Reaction pathway diagram of L-His-Fe$_3$O$_4$.

TEM images demonstrated spherical particles of L-His-Fe$_3$O$_4$ with a diameter of approximately 20 nm, primarily composed of Fe and O elements. The selected area electron diffraction (SAED) pattern (Figure 1c) of L-His-Fe$_3$O$_4$ confirms the apparent diffraction rings, which correspond to the (440) (511) (400), and (311) crystal planes. To confirm the efficiency of the synthesis method, X-ray diffraction (XRD) analysis was used to monitor the crystal phase at different reaction times. As shown in Figure 1d, the diffraction peaks of the product at 1 min aligned well with those of Fe$_3$O$_4$ (PDF#19–0,629). After 3, 6, and 12 h of reaction, the crystal phase remained unchanged, indicating the high efficiency of the synthesis method. The particle size distribution of L-His-Fe$_3$O$_4$ ranged from 200 to 800 nm (Figure 1e), and the zeta potential varied with changes in pH (Figure 1f). The generation of oxygen vacancies (OVs) in L-His-Fe$_3$O$_4$ was measured by electron paramagnetic resonance (EPR). The g = 2.003 and the peak with magnetic field at around 3,500 revealed that L-His-Fe$_3$O$_4$ possessed at ypical signal of Ovs (Figures 1g, h).

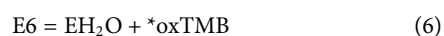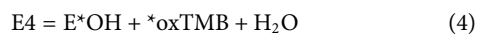## 3.2 Enzyme activity characterization and theoretical calculation

To assess the peroxidase -like activity of L-His-Fe$_3$O$_4$, the absorption intensity of the L-His-Fe$_3$O$_4$ nanozyme-catalyzed TMB colorimetric reaction at 652 nm was measured (Figure 2a). The absorbance intensity of oxidized TMB (ox-TMB) increased over time. Furthermore, compared with Fe$_3$O$_4$, L-His-Fe$_3$O$_4$ exhibited higher POD-like activity. The generation of •OH radicals was monitored using electron spin resonance (ESR) spectroscopy, and the results (Figure 2b) showed a significant increase in •OH signal intensity, indicating that L-His-Fe$_3$O$_4$ could effectively catalyze the formation of •OH from H$_2$O$_2$.

To investigate L-His's role in the catalytic reduction of H$_2$O$_2$ from an electronic structure perspective, we conducted electrostatic potential analysis, density of states analysis, and differential charge density mapping before and after L-His modification of the surface. Electrostatic potential analysis on the Fe$_3$O (311) surface was

performed before and after L-His adsorption (Figure 2c). Red regions indicate positive electrostatic potential, while blue regions indicate negative electrostatic potential. These results demonstrate that the modification increased the polarity of the Fe_3O_4 surface, facilitating the reaction between Fe_3O_4 and H_2O_2 during TMB oxidation.

Density of states plots for the slab model of the Fe_3O_4 (311) surface before and after L-His adsorption is shown in Figures 2d, e. The results indicate that L-His modification led to a more continuous distribution of states near the Fermi level in Fe_3O_4, enhancing electron transfer during the catalytic process, reducing the energy barrier, and promoting the reaction (Supplementary Figure S1). Differential charge density maps for H_2O_2 adsorption on the Fe_3O_4 (311) surface before and after L-His modification is presented in Supplementary Figure S2. The modification increased the interaction between the Fe_3O_4 surface and H_2O_2, with differential charge density results also indicating enhanced charge exchange between the modified Fe_3O_4 (311) surface and H_2O_2. According to Coulomb's law, this intensifies the interaction between the two.

To evaluate the impact of modification on Fe_3O_4's catalytic process in the oxidation of TMB by H_2O_2, we calculated the energy changes throughout the reaction, as shown in Figures 2e, f. Steps one to six correspond to the stages in the reaction pathway diagram, with "*" denoting the adsorption state on the catalyst surface. Oxidized TMB (oxTMB) refers to TMB in its oxidized form after hydrogen loss (Figure 2f) (Equations 1-6).

$$E1 = Eslab = 0 \tag{1}$$

$$E2 = E^*H_2O_2 \tag{2}$$

$$E3 = E^*H_2O_2 + {}^*TMB \tag{3}$$

$$E4 = E^*OH + {}^*oxTMB + H_2O \tag{4}$$

$$E5 = E^*OH + {}^* oxTMB \tag{5}$$

$$E6 = EH_2O + {}^*oxTMB \tag{6}$$

The calculations revealed that: (1) Compared to the unmodified Fe_3O_4 surface, the binding energy of L-His-modified Fe_3O_4 with H_2O_2 is more negative, indicating a stronger interaction between the modified Fe_3O_4 surface and H_2O_2, which facilitates H_2O_2 activation during catalysis; (2) The energy barrier during the reaction process, occurring in the reduction of H_2O_2 to ?OH by TMB, was significantly lowered from 5.7058 eV to 1.2987 eV with L-His modification, greatly enhancing the reaction progress.

3.3 The anti-bacterial activity of L-His-Fe$_3$O$_4$ against *S. aureus* and *E. coli*

Nanozymes with peroxidase (POD)-like enzyme activity can catalyze H_2O_2 to produce •OH, a ROS that induces bacterial cell death. The combination of nanozyme and H_2O_2 represents the primary mechanism of the antibacterial effect of nanozymes. To achieve a satisfactory antibacterial effect, we selected L-His-Fe$_3$O$_4$, which has high POD-like activity, for further investigation of its antibacterial performance in the presence of H_2O_2. To mitigate the toxicity of high H_2O_2 concentrations, we used a concentration much lower than the clinically effective range (0.5%–3%, wt%). The experimental results are shown in Figure 3B Following L-His

modification, the antibacterial effect of Fe_3O_4 was significantly enhanced, with efficacy increasing proportionally with concentration (Figure 3a). Results in Figure 3b demonstrate that treating *S. aureus* with H_2O_2 or L-His-Fe$_3$O$_4$ (100 μg/mL) alone reduced bacterial counts by approximately 0.5 lg (CFU/mL) compared to the control. However, combining L-His-Fe$_3$O$_4$ (100 μg/mL) with H_2O_2 (L-His-Fe$_3$O$_4$/H_2O_2) reduced bacterial counts by 3.04 lg (CFU/mL). Additionally, the morphology of *S. aureus* after L-His-Fe$_3$O$_4$ treatment showed noticeable damage (Supplementary Figures S3, S4). Similar effects were observed in the elimination of other Gram-negative bacteria, such as *E. coli* (Figure 3c). Post L-His-Fe$_3$O$_4$ treatment, laser confocal microscopy revealed a significant increase in the proportion of dead cells within the *S. aureus* biofilm (Figure 3d), corresponding fluorescence intensity analysis of Figure 3d (Supplementary Figure S5). Along with a marked reduction in crystal violet staining and biofilm dry weight compared with the control (Figures 3e, f). The lipid oxidation fluorescent ratio-probe DCFH-DA indicated increased lipid ROS when *S. aureus* was treated with L-His-Fe$_3$O$_4$ (Figure 3g). ANS as a fluorescent probe can be used to detect membrane permeability. Fluorescence monitoring of ANS dye in *S. aureus* cells before and after L-His-Fe$_3$O$_4$ treatment revealed a significant increase in membrane permeability (Figure 3h). Using the membrane potential-sensitive probe DiSC3, we observed that L-His-Fe$_3$O$_4$ depolarized the *S. aureus* cell membrane, resulting in enhanced fluorescence (Figure 3i), indicating a reduction in membrane potential as DiSC3(5) was released into the solution upon membrane depolarization. This suggested that L-His-Fe$_3$O$_4$ interacted with the bacterial cell membrane, disrupting its integrity and leading to oxidative stress and cell death.

3.4 Biosafety studies in vitro and in vivo

Good biocompatibility is essential for the *in vivo* and *in vitro* applications of L-His-Fe$_3$O$_4$. The hemolysis rate is a key indicator of material biocompatibility; thus, human red blood cells were used in a hemolysis test. As shown in Figures 4a, b, even at the highest concentrations of Fe_3O_4 and L-His-Fe$_3$O$_4$, the hemolysis rate remained below 1%. The viability of HaCaT cells incubated with various concentrations of L-His-Fe$_3$O$_4$ was assessed using a CCK-8 assay, revealing that cell viability remained above 95% across all concentrations (Figure 4c). To further evaluate the *in vivo* safety of L-His-Fe$_3$O$_4$, mice were treated with L-His-Fe$_3$O$_4$ for 7 days. After treatment, several major organs (heart, liver, spleen, lungs, kidneys) were collected, fixed in 4% neutral formaldehyde, and subjected to histopathological analysis with H&E staining. No lesions were detected in any of the groups, underscoring the biosafety of L-His-Fe$_3$O$_4$ (Figure 4d).

3.5 Evaluation of antibacterial properties *in vivo*

To further investigate the antibacterial efficacy of L-His-Fe$_3$O$_4$ and its potential to promote wound healing, we established a skin wound model of MRSA-infected mice with reference to the experimental method of Liu (Liu et al., 2023). Throughout
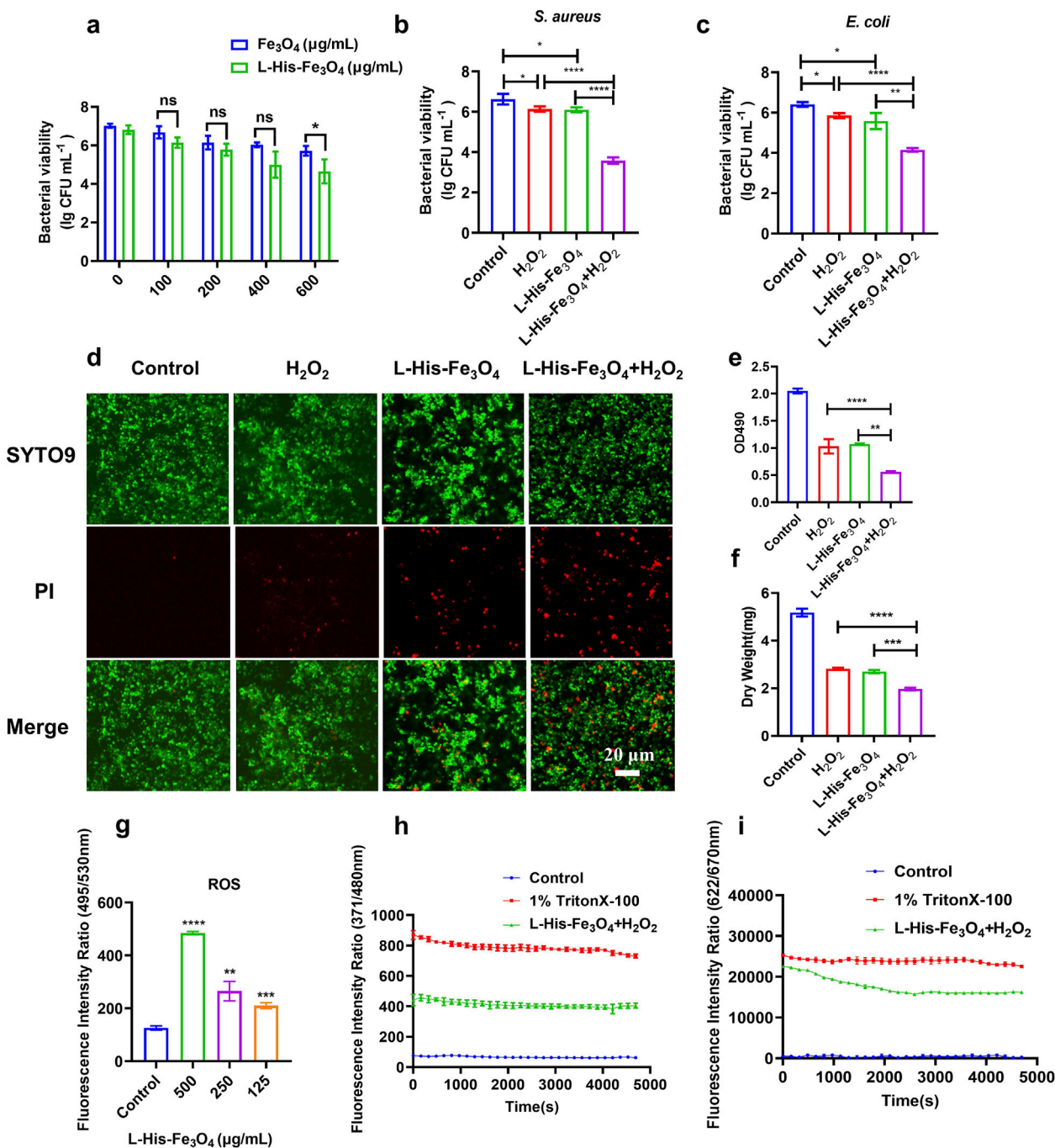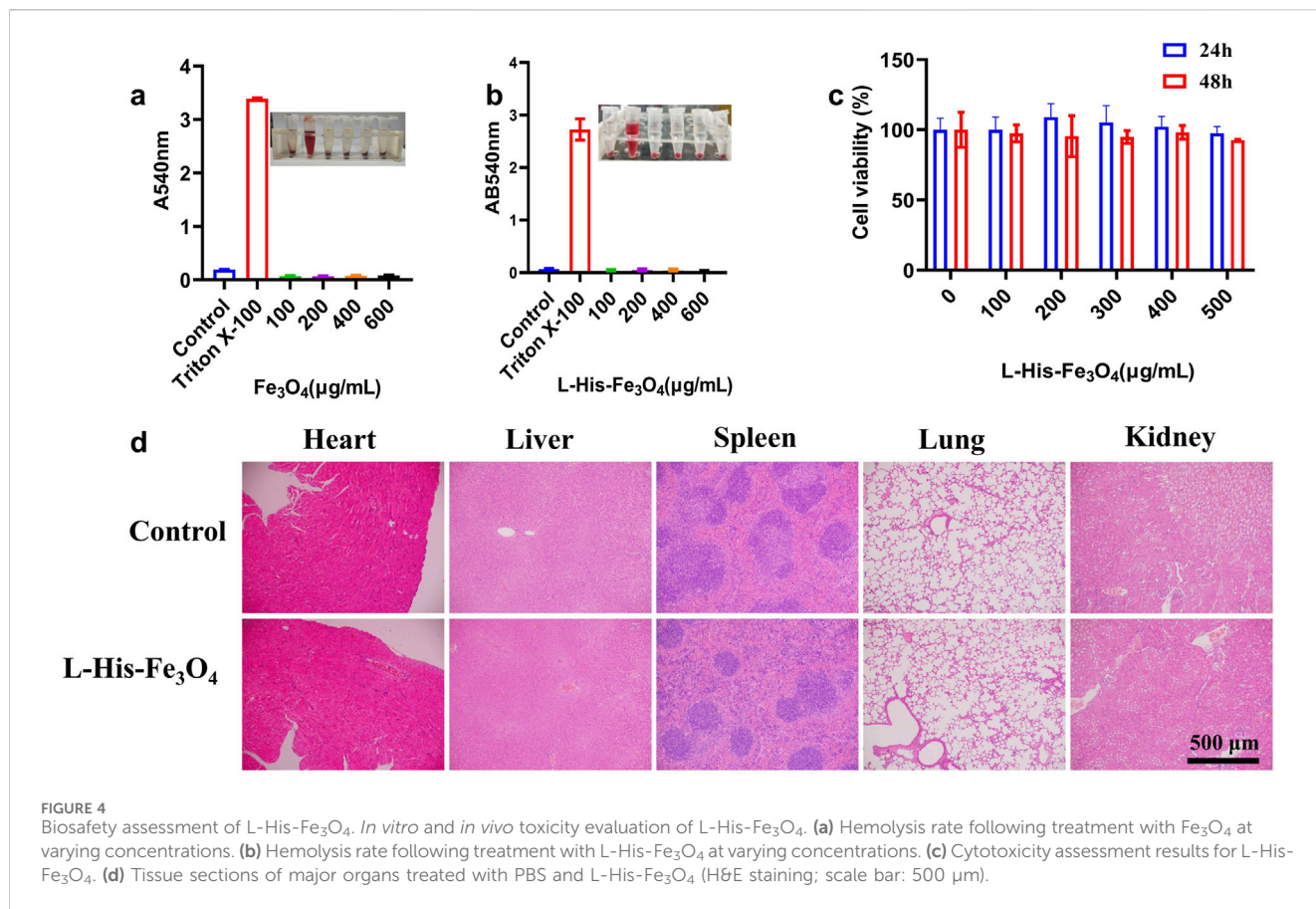
FIGURE 3
Test of antibacterial property and bactericidal mechanism of L-His-Fe$_3$O$_4$. **(a)** Measurement of *S. aureus* viability with varying concentrations of L-His-Fe$_3$O$_4$ and Fe$_3$O$_4$. b-c. Viability of *S. aureus* **(b)** and *E. coli* **(c)** treated with H$_2$O$_2$ + L-His-Fe$_3$O$_4$. **(d)** Impact of L-His-Fe$_3$O$_4$ on *S. aureus* biofilm viability (Scale bar: 20 μm). **(e)** Crystal violet staining of *S. aureus* biofilm treated with L-His-Fe$_3$O$_4$. **(f)** Dry weight of *S. aureus* biofilm treated with L-His-Fe$_3$O$_4$. **(g)** ROS levels in *S. aureus* treated with L-His-Fe$_3$O$_4$. **(h)** Outer membrane permeabilization by L-His-Fe$_3$O$_4$. **(i)** Cytoplasmic membrane depolarization by L-His-Fe$_3$O$_4$. The data are presented as the means ± SD. *p < 0.05, **p < 0.01, ***p < 0.001, ****p < 0.0001.

treatment, wound changes were documented with photographs. As shown in Figure 5a, all experimental groups exhibited gradual scab formation and wound contraction. On day 7, the control and Vancomycin groups displayed severe purulent symptoms, whereas the H$_2$O$_2$ and L-His-Fe$_3$O$_4$ + H$_2$O$_2$ groups showed no purulence and began to scab. By day 9, scabs started forming in the control and Vancomycin groups, while those in the H$_2$O$_2$ and

L-His-Fe$_3$O$_4$ + H$_2$O$_2$ groups began to peel off. On day 11, the wounds in the L-His-Fe$_3$O$_4$ + H$_2$O$_2$ group were significantly smaller than those in the other groups. To evaluate wound healing, H&E and Masson staining were performed on the wound tissues. As shown in Figure 5b, after 11 days of treatment, the control, Vancomycin, and H$_2$O$_2$ groups displayed incomplete epidermal layers, while the treatment group showed uniformly distributed collagen fibers.

FIGURE 4
Biosafety assessment of L-His-Fe$_3$O$_4$. *In vitro* and *in vivo* toxicity evaluation of L-His-Fe$_3$O$_4$. **(a)** Hemolysis rate following treatment with Fe$_3$O$_4$ at varying concentrations. **(b)** Hemolysis rate following treatment with L-His-Fe$_3$O$_4$ at varying concentrations. **(c)** Cytotoxicity assessment results for L-His-Fe$_3$O$_4$. **(d)** Tissue sections of major organs treated with PBS and L-His-Fe$_3$O$_4$ (H&E staining; scale bar: 500 μm).

Additionally, we monitored the weight changes in each group during treatment (Figure 5c), finding no significant weight differences among the groups. On day 7, three mice from each group were selected, and the wound tissues were ground and subjected to plate counting; the results are shown in Figure 5d. The L-His-Fe$_3$O$_4$ + H$_2$O$_2$ treatment group exhibited significantly stronger antibacterial effects than the other groups, confirming that the treatment of infected wounds in mice with L-His-Fe$_3$O$_4$ + H$_2$O$_2$ is effective.

4 Discussion

With the increasing of antibiotic resistance in the world, the search for new antimicrobial agents has become a hot spot in today's research (Dance, 2024). As a kind of antibacterial agent with high efficiency, selectivity and biocompatibility, nanozymes have received extensive attention (Labrag et al., 2023; Chakraborty et al., 2022). Among them, Fe$_3$O$_4$ nano-enzyme has become the focus of research because of its excellent performance and wide application prospect. In 2007, Gao et al. (2007) first identified magnetic iron oxide nanoparticles (Fe$_3$O$_4$ nanoparticles) with significant enzyme-like activity. Studies showed that Fe$_3$O$_4$ had a pH-dependent peroxide-like activity and catalase activity. In particular, Fe$_3$O$_4$ effectively catalyzes hydrogen peroxide to produce hydroxyl radicals in acidic conditions, which is antibacterial and kills tumor cells (Gao et al., 2016; Shi et al., 2018). Although Fe$_3$O$_4$ nanoenzymes have broad application prospects in biomedicine, there are still some challenges. Firstly, the synthesis method of Fe$_3$O$_4$ nanozymes need to be further

optimized to improve their yield and stability. This study provides a convenient and rapid synthesis method for Fe$_3$O$_4$ at room temperature, supports large-scale production, and has important application prospects in the field of antibacterial.

The commonly used methods for preparing Fe$_3$O$_4$ include chemical coprecipitation, thermal decomposition, sol-gel, mechanical synthesis and oil phase coprecipitation (Yang et al., 2011). However, the existing preparation methods still have some defects: the preparation process is complicated, multiple parameters need to be controlled, and the preparation cycle is long (Wang et al., 2024). For example, hydrothermal synthesis of Fe$_3$O$_4$ often requires a high temperature of more than 200°C in a closed high-pressure reactor for 12 h (Gao et al., 2007), which requires high equipment and complex operation, which may cause certain pressure and safety hazards to the environment. We have synthesized L-His-Fe$_3$O$_4$ at room temperature by an improved method, L-His-Fe$_3$O$_4$ was quickly synthesized by stirring at room temperature for 1 min. TEM images show that L-His- Fe$_3$O$_4$ is a spherical particle with a diameter of about 20 nm, mainly composed of iron and oxygen elements (Figure 1). This method is simple to operate, the prepared iron oxide nanoparticles are of high quality and the end modification is flexible.

As a commonly used high reactive oxygen species, H$_2$O$_2$ has been widely used to prevent and control the infection of various pathogenic microorganisms. However, high doses of H$_2$O$_2$ can cause unnecessary damage to normal tissue, delaying healing. Fe$_3$O$_4$ nanozymes have peroxisase-like activity, which can promote the transformation of H$_2$O$_2$ to OH, and have great potential in tumor
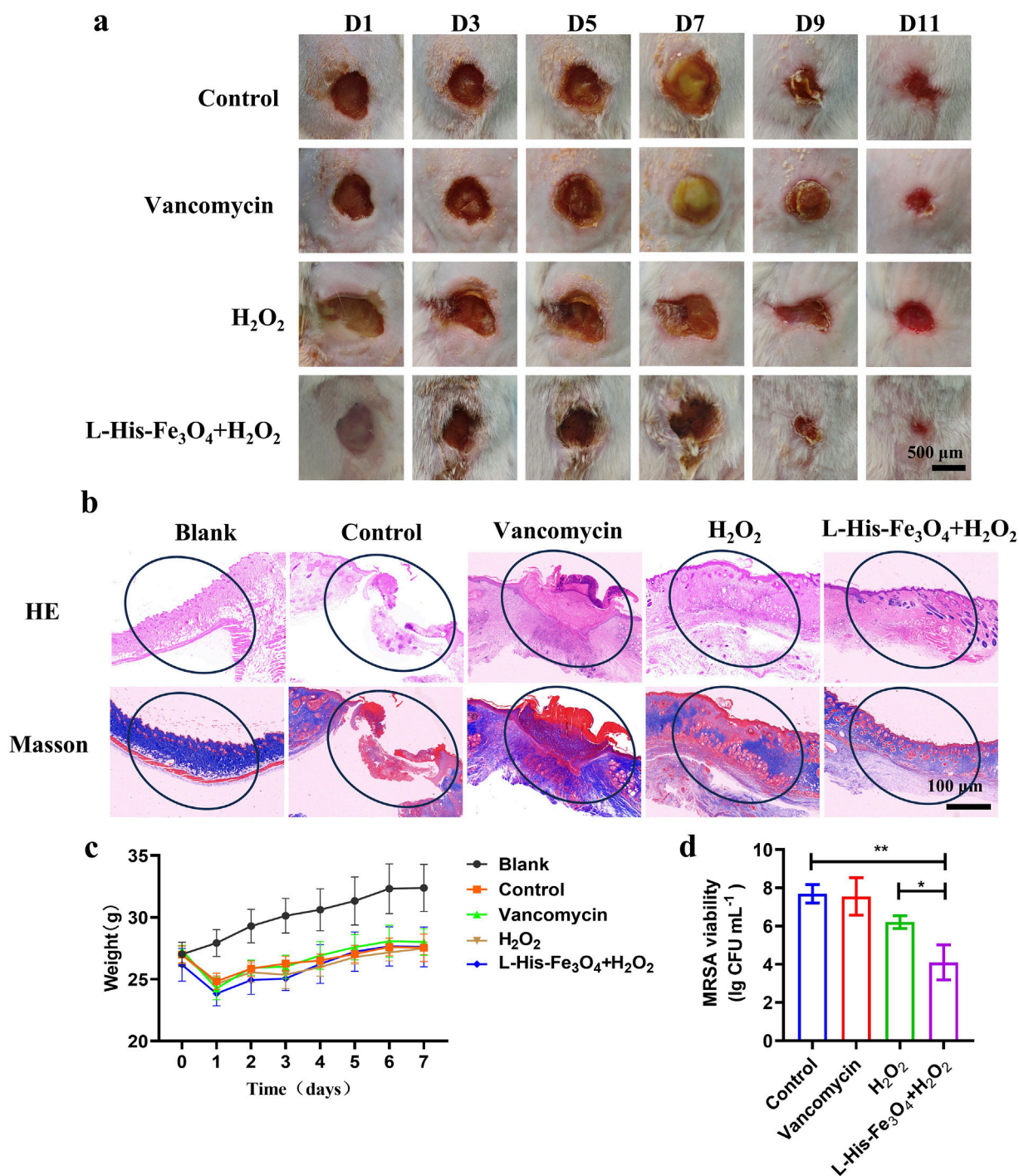
FIGURE 5
Application evaluation of bacterial infection in skin wounds. **(a)** Wound area of mice treated with PBS, Vancomycin, H_2O_2 and L-His-Fe_3O_4 over time. **(b)** H&E (top) and Masson staining (bottom) of infected tissues following different treatments. **(c)** Changes in body weight of mice over time with various treatments (n = 5) **(d)** Residual bacterial counts in wound tissue after different treatments. The data are presented as the means $\pm$ SD. *p < 0.05, **p < 0.01.

catalytic therapy and antimicrobial resistance (Zarandona et al., 2023; Anghel et al., 2014). Fe_3O_4 nanozymes with enzyme properties can effectively improve the antibacterial performance of H_2O_2, while avoiding the side effects of high concentration of H_2O_2, and become a promising antibacterial agent (Uwaya et al., 2020). We report a novel strategy for the rapid synthesis of Fe_3O_4 nanozymes by adding L-His. We demonstrated that L-His- Fe_3O_4 can be used to kill

resistant bacteria such as *S. aureus* and *E. coli*, destroy biofilm (Figure 3). Animal experiments demonstrated the potential of L-His- Fe_3O_4 as a multifunctional material for wound infections (Figure 5).

In summary, this study demonstrates the synthesis of L-His-Fe_3O_4 using an ultrafast, low-cost method at room temperature. The addition of L-His significantly enhanced POD-like activity, endowing L-His-

Fe_3O_4 with excellent antibacterial efficacy against *S. aureus* and *E. coli*. Following L-His modification, the antibacterial rate against *S. aureus* increased from 72.72% to 99.92%. The antibacterial effect relied on the POD-like activity of L-His-Fe_3O_4, which generated •OH to damage bacterial cell membranes. Cytotoxicity assessments via CCK-8 and red blood cell hemolysis tests confirmed high biosafety. *In vivo* experiments demonstrated a substantial therapeutic effect of L-His-Fe_3O_4 on bacteria-infected wounds. The synthesis method preserves the integrity of amino acids and can be applied to modify various functional groups, suggesting it as a potentially universal approach. This study offers a convenient and rapid synthesis method for Fe_3O_4, supporting large-scale production and presenting significant promise for future applications in the antibacterial field.

Data availability statement

The original contributions presented in the study are included in the article/Supplementary Material, further inquiries can be directed to the corresponding authors.

Ethics statement

Ethical approval was not required for the studies on humans in accordance with the local legislation and institutional requirements because only commercially available established cell lines were used. The animal study was approved by Life Science Ethics Review Committee, Zhengzhou University: GZR 2022-1328. The study was conducted in accordance with the local legislation and institutional requirements.

Author contributions

Funding

Conflict of interest

The authors declare that the research was conducted in the absence of any commercial or financial relationships that could be construed as a potential conflict of interest.

Generative AI statement

The author(s) declare that no Generative AI was used in the creation of this manuscript.

Publisher's note

All claims expressed in this article are solely those of the authors and do not necessarily represent those of their affiliated organizations, or those of the publisher, the editors and the reviewers. Any product that may be evaluated in this article, or claim that may be made by its manufacturer, is not guaranteed or endorsed by the publisher.

Supplementary material

The Supplementary Material for this article can be found online at: https://www.frontiersin.org/articles/10.3389/fbioe.2025.1548025/full#supplementary-material

References

Alim-Marvasti, A., Bi, W., Mahroo, O. A., Barbur, J. L., and Plant, G. T. (2016). Transient smartphone blindness. *N. Engl. J. Med.* 374, 2502–2504. doi:10.1056/NEJMc1514294

Anghel, A. G., Grumezescu, A., Chirea, M., Grumezescu, V., Socol, G., Iordache, F., et al. (2014). MAPLE fabricated Fe3O4@Cinnamomum verum antimicrobial surfaces for improved gastrostomy tubes. *Molecules* 19, 8981–8994. doi:10.3390/molecules19078981

Brown, E. D., and Wright, G. D. (2016). Antibacterial drug discovery in the resistance era. *Nature* 529, 336–343. doi:10.1038/nature17042

Brussow, H. (2024). The antibiotic resistance crisis and the development of new antibiotics. *Microb. Biotechnol.* 17, e14510. doi:10.1111/1751-7915.14510

Burki, T. K. (2018). Superbugs: an arms race against bacteria. *Lancet Respir. Med.* 6, 668. doi:10.1016/S2213-2600(18)30271-6

Chakraborty, N., Gandhi, S., Verma, R., and Roy, I. (2022). Emerging prospects of nanozymes for antibacterial and anticancer applications. *Biomedicines* 10, 1378. doi:10.3390/biomedicines10061378

Dance, A. (2024). Five ways science is tackling the antibiotic resistance crisis. *Nature* 632, 494–496. doi:10.1038/d41586-024-02601-4

Dong, H., Du, W., Dong, J., Che, R., Kong, F., Cheng, W., et al. (2022). Depletable peroxidase-like activity of Fe(3)O(4) nanozymes accompanied with separate migration of electrons and iron ions. *Nat. Commun.* 13, 5365. doi:10.1038/s41467-022-33098-y

Du, Y., Ke, Z., Zhang, J., and Feng, G. (2022). Dual-signal output paper sensor based on coordinative self-assembly biomimetic nanozyme for point-of-care detection of biomarker. *Biosens. Bioelectron.* 216, 114656. doi:10.1016/j.bios.2022.114656

Fan, X., Yang, F., Nie, C., Ma, L., Cheng, C., and Haag, R. (2021). Biocatalytic nanomaterials: a new pathway for bacterial disinfection. *Adv. Mater* 33, e2100637. doi:10.1002/adma.202100637

Gao, L., Liu, Y., Kim, D., Li, Y., Hwang, G., Naha, P. C., et al. (2016). Nanocatalysts promote Streptococcus mutans biofilm matrix degradation and enhance bacterial killing to suppress dental caries *in vivo*. *Biomaterials* 101, 272–284. doi:10.1016/j.biomaterials.2016.05.051

Gao, L., Wei, H., Dong, S., and Yan, X. (2024). Nanozymes. *Adv. Mater* 36, e2305249. doi:10.1002/adma.202305249

Gao, L., Zhuang, J., Nie, L., Zhang, J., Zhang, Y., Gu, N., et al. (2007). Intrinsic peroxidase-like activity of ferromagnetic nanoparticles. *Nat. Nanotechnol.* 2, 577–583. doi:10.1038/nnano.2007.260

Gupta, A., Mumtaz, S., Li, C. H., Hussain, I., and Rotello, V. M. (2019). Combatting antibiotic-resistant bacteria using nanomaterials. *Chem. Soc. Rev.* 48, 415–427. doi:10.1039/c7cs00748e

He, W., Kim, H. K., Wamer, W. G., Melka, D., Callahan, J. H., and Yin, J. J. (2014). Photogenerated charge carriers and reactive oxygen species in ZnO/Au hybrid nanostructures with enhanced photocatalytic and antibacterial activity. *J. Am. Chem. Soc.* 136, 750–757. doi:10.1021/ja410800y

Jiang, D., Ni, D., Rosenkrans, Z. T., Huang, P., Yan, X., and Cai, W. (2019). Nanozyme: new horizons for responsive biomedical applications. *Chem. Soc. Rev.* 48, 3683–3704. doi:10.1039/c8cs00718g

Labrag, J., Abbadi, M., Hnini, M., Bekkali, C. E., Bouziani, A., Robert, D., et al. (2023). Antibiotic photocatalysis and antimicrobial activity of low-cost multifunctional Fe(3) O(4)@HAp nanocomposites. *J. Environ. Health Sci. Eng.* 21, 429–440. doi:10.1007/s40201-023-00869-8

Lee, A., Xie, Y. L., Barry, C. E., and Chen, R. Y. (2020). Current and future treatments for tuberculosis. *BMJ* 368, m216. doi:10.1136/bmj.m216

Li, X., Bai, H., Yang, Y., Yoon, J., Wang, S., and Zhang, X. (2019). Supramolecular antibacterial materials for combatting antibiotic resistance. *Adv. Mater* 31, e1805092. doi:10.1002/adma.201805092

Liu, Q., Liu, X., He, X., Wang, D., Zheng, C., Jin, L., et al. (2024). Iron-single-atom nanozyme with NIR enhanced catalytic activities for facilitating MRSA-infected wound therapy. *Adv. Sci. (Weinh)* 11, e2308684. doi:10.1002/advs.202308684

Liu, Q., Wan, K., Shang, Y., Wang, Z. G., Zhang, Y., Dai, L., et al. (2021). Cofactor-free oxidase-mimetic nanomaterials from self-assembled histidine-rich peptides. *Nat. Mater* 20, 395–402. doi:10.1038/s41563-020-00856-6

Liu, Y., Wang, X., Fan, X., Ge, M., Fang, L., Yuan, Y., et al. (2023). Coordination-precipitation synthesis of metal sulfide with phase transformation enhanced reactivity against antibiotic-resistant bacteria. *Adv. Funct. Mater.* 33. doi:10.1002/adfm.202212655

Makabenta, J. M. V., Nabawy, A., Li, C. H., Schmidt-Malan, S., Patel, R., and Rotello, V. M. (2021). Nanomaterial-based therapeutics for antibiotic-resistant bacterial infections. *Nat. Rev. Microbiol.* 19, 23–36. doi:10.1038/s41579-020-0420-1

Panda, S., Rout, T. K., Prusty, A. D., Ajayan, P. M., and Nayak, S. (2018). Electron transfer directed antibacterial properties of graphene oxide on metals. *Adv. Mater* 30. doi:10.1002/adma.201702149

Pogue, J. M., Kaye, K. S., Cohen, D. A., and Marchaim, D. (2015). Appropriate antimicrobial therapy in the era of multidrug-resistant human pathogens. *Clin. Microbiol. Infect.* 21, 302–312. doi:10.1016/j.cmi.2014.12.025

Seaberg, J., Clegg, J. R., Bhattacharya, R., and Mukherjee, P. (2023). Self-therapeutic nanomaterials: applications in biology and medicine. *Mater TodayKidlingt.* 62, 190–224. doi:10.1016/j.mattod.2022.11.007

Sheng, J., Wu, Y., Ding, H., Feng, K., Shen, Y., Zhang, Y., et al. (2024). Multienzyme-like nanozymes: regulation, rational design, and application. *Adv. Mater* 36, e2211210. doi:10.1002/adma.202211210

Shi, S., Wu, S., Shen, Y., Zhang, S., Xiao, Y., He, X., et al. (2018). Iron oxide nanozyme suppresses intracellular Salmonella Enteritidis growth and alleviates infection *in vivo*. *Theranostics* 8, 6149–6162. doi:10.7150/thno.29303

Song, N., Yu, Y., Zhang, Y., Wang, Z., Guo, Z., Zhang, J., et al. (2024). Bioinspired hierarchical self-assembled nanozyme for efficient antibacterial treatment. *Adv. Mater* 36, e2210455. doi:10.1002/adma.202210455

Theuretzbacher, U., Outterson, K., Engel, A., and Karlen, A. (2020). The global preclinical antibacterial pipeline. *Nat. Rev. Microbiol.* 18, 275–285. doi:10.1038/s41579-019-0288-0

Trujillo-Alonso, V., Pratt, E. C., Zong, H., Lara-Martinez, A., Kaittanis, C., Rabie, M. O., et al. (2019). FDA-approved ferumoxytol displays anti-leukaemia efficacy against cells with low ferroportin levels. *Nat. Nanotechnol.* 14, 616–622. doi:10.1038/s41565-019-0406-1

Uwaya, G. E., Fayemi, O. E., Sherif, E. M., Junaedi, H., and Ebenso, E. E. (2020). Synthesis, electrochemical studies, and antimicrobial properties of Fe(3)O(4) nanoparticles from callistemon viminalis plant extracts. *Mater. (Basel)* 13, 4894. doi:10.3390/ma13214894

Wang, X., Liu, T., Chen, M., Liang, Q., Jiang, J., Chen, L., et al. (2024). An erythrocyte-templated iron single-atom nanozyme for wound healing. *Adv. Sci. (Weinh)* 11, e2307844. doi:10.1002/advs.202307844

Wang, Y., Sun, S., Zhang, Z., and Shi, D. (2018). Nanomaterials for cancer precision medicine. *Adv. Mater* 30, e1705660. doi:10.1002/adma.201705660

Wei, F., Cui, X., Wang, Z., Dong, C., Li, J., and Han, X. (2021). Recoverable peroxidase-like Fe(3)O(4)@MoS(2)-Ag nanozyme with enhanced antibacterial ability. *Chem. Eng. J.* 408, 127240. doi:10.1016/j.cej.2020.127240

Xie, L., Wu, H., Li, Y., Shi, L., and Liu, Y. (2024). Recent development of nanozymes for combating bacterial drug resistance: a review. *Adv. Healthc. Mater*, e2402659. doi:10.1002/adhm.202402659

Yang, C., Wu, J., and Hou, Y. (2011). Fe3O4 nanostructures: synthesis, growth mechanism, properties and applications. *Chem. Commun. (Camb)* 47, 5130–5141. doi:10.1039/c0cc05862a

Yang, M., He, H., Du, J., Peng, H., Ke, G., and Zhou, Y. (2019). Insight into the kinetic influence of oxygen vacancies on the WO(3) photoanodes for solar water oxidation. *J. Phys. Chem. Lett.* 10, 6159–6165. doi:10.1021/acs.jpclett.9b02365

Zarandona, I., Correia, D. M., Moreira, J., Costa, C. M., Lanceros-Mendez, S., Guerrero, P., et al. (2023). Magnetically responsive chitosan-pectin films incorporating Fe(3)O(4) nanoparticles with enhanced antimicrobial activity. *Int. J. Biol. Macromol.* 227, 1070–1077. doi:10.1016/j.ijbiomac.2022.11.286